Journal of Alloys and Compounds 509 (2011) 6467–6475

Contents lists available at ScienceDirect

Journal of Alloys and Compounds

journal homepage: www.elsevier.com/locate/jallcom

Structural and optical characterizations of pyronine B thin films and its photovoltaic applications

A.A.M. Farag[a,*], W.G. Osiris[b], E.A.A. El-Shazly[a]

[a] Physics Department, Faculty of Education, Ain Shams University, Roxy, Cairo, Egypt
[b] Biophysics Department, Faculty of Science, Cairo University, Cairo, Egypt

ARTICLE INFO

Article history:
Received 17 December 2010
Received in revised form 13 March 2011
Accepted 16 March 2011
Available online 23 March 2011

Keywords:
Pyronine B
Optical properties
Electrical properties
Photovoltaics

ABSTRACT

In this work, the organic thin films of pyronine B (PYR.B) were deposited by thermal evaporation technique under high vacuum (~10^4 Pa). The crystal structure, examined by X-ray powder diffraction, indicates that the films are single phase with strong preferred (4 0 0) orientation. Scanning electron micrographs of the films indicate a clearly almost uniform distribution with large grain sizes in the range 5–10 μm. The molecular structure and electronic transitions of PYR.B were investigated by Fourier-transform infrared (FTIR). Fluorescence characteristic of PYR.B at room temperature (300 K) exhibits visible band peak located at 569.65 nm. The color parameters were extracted from the reflectance spectrum of PYR.B. The optical constants such as refractive and extinction indices were determined from the measured transmittance and reflectance spectra using the spectrophotometric method. The dependence of absorption coefficient on the photon energy was determined and the analysis of the result showed that the optical transition in PYR.B is allowed and direct. The current density–voltage (*J–V*) characteristics in dark show the rectification effect due to the formation of Schottky barrier at Al/PYR.B interface. The photovoltaic parameters were calculated from the *J–V* characteristics under illumination through ITO and discussed in detail.

1. Introduction

Organic materials that have semiconducting properties are of particular interest, since they possess advantageous electrical, optoelectronic and processing properties for design and fabrication of novel class of the semiconductor-based devices such as diodes, photovoltaic devices [1]. Moreover, they have advantages of low cost, ease of processing, and the ability to modify their structure to obtain the desired electrical and optical characteristics when compared with conventional inorganic semiconductors [2–6].

Many advanced technologies, especially in electronic and optoelectronic devices, require thin layers of new functional materials with special optical and electrical properties [7–10]. Such properties are determined by a complex combination of many physical factors as well as the chemical nature of the starting material. Organic semiconducting layers are one of such class of prospective thin layer materials [11–13]. Their low cost production is very simple using recent high vacuum evaporation and spin coating technology and their optical and electrical properties can be modified over a wide range [7–13]. The physical and chemical properties of these material layers depend not only on the molecular structure but also on the structure of the solid thin film [13–15].

The specific electrical and optical properties of organic semiconductor layer are of special interest, e.g. the absorption of light energy in the thin layer can be converted into electrical, chemical and thermal energy, leading to some interesting applications such as solar cells nonlinear optical devices [7,16], luminescence devices [16,17] and energy conversion and storage devices [18–20]. Much research has been carried out on the use of these organic semiconductors as active element for these devices [13–15,7,16–20].

Xanthene dyes such as PYR.B have high absorption coefficient and are easily processed and can be functionalized to obtain the specific optical and electrical properties [21,22]. Owing to these properties, xanthene dyes are widely used, especially for dye lasers [23] solar energy conversion devices [24] photosensitizer compounds for chemical reactions [25,26] and nonlinear optical media for many applications [24–26].

In the present study, the thermal evaporation technique was performed to prepare organic thin films of PYR.B on glass, ITO-coated glass and quartz substrates. The structure and surface morphology of thin films were investigated using XRD and SEM. The color parameters were calculated from the reflectance spectrum. Optical constants such as refractive index, extinction coefficient and dielectric constant were determined from the measured

* Corresponding author. Tel.: +20 233518705; fax: +20 222581243.
E-mail address: alaafaragg@yahoo.com (A.A.M. Farag).

0925-8388/$ – see front matter © 2011 Elsevier B.V. All rights reserved.
doi:10.1016/j.jallcom.2011.03.096

Fig. 1. Molecular structure of PYR.B.

transmittance and reflectance spectra. The photovoltaic characterizations were measured using the sandwich structure of Al/PYR.B/ITO. Various electrical and photoelectrical parameters were also determined from the analyses of *J–V* characteristics in dark and under illumination.

2. Experimental procedures

2.1. Materials and preparation

Pyronine B (PYR.B) powder was supplied from Aldrich company. The molecular structure of PYR.B is shown in Fig. 1. Thin films of PYR.B were prepared by thermal evaporation technique [27], using a high vacuum coating unit (Edward, E306A). The films were evaporated from quartz crucible source charged by PYR.B and heated by a tungsten coil in a vacuum of 10^{-4} Pa during deposition. The films were deposited onto pre-cleaned optically flat quartz and glass coated ITO substrates maintained at room temperature (300 K) and the deposition rate was controlled by using a quartz crystal thickness monitor (Edwards, FTM4).

2.2. Measurements

The structural characterization was investigated by using the obtained X-ray diffraction patterns (XRD). A Philips X-Ray Diffractometer (model X' pert) was used for the measurements with utilized monochromatic CuK_α radiation operated at 40 kV and 25 mA. The diffraction patterns were recorded automatically with a scanning speed of 2° min^{-1} in the 2θ range 10–60°.

The surface morphology of the PYR.B was checked from the scanning electron micrograph images obtained from Scanning Electron Microscope, SEM (Model JXA 8400, JEOL, Japan).

The infrared transmission spectra of the prepared samples were measured at room temperature in the range 4000–400 cm^{-1} by an infrared spectrometer (ATI Mattson Infrared Spectrophotometer) using the KBr as reference material. The KBr discs were subjected to a load of 5 tons cm^{-2} for 2 min to produce clear homogenous discs. The PYR.B film was prepared on KBr using the thermal evaporation method. The IR absorption spectrum was measured immediately after preparing the discs.

Fluorescence measurements were performed on a Fluorescence Spectrometer (Perkin Elmer L550B, Wellesley, MA, USA), employing a 500 W Hg–Xe high pressure lamp. The concentration of PYR.B was measured in ethanol solution at 0.5×10^{-5} mol L^{-1}.

The measurements of the transmittance $T(\lambda)$ and reflectance, $R(\lambda)$ were carried out using a Double Beam Spectrophotometer model (type JASCO, V-570, UV-VIS-NIR, Japan) at normal incidence of light in the wavelength range 190–2500 nm. An uncertainty of 1% was given by the manufacturer for the measurements obtained by this spectrophotometer. A blank optically flat quartz substrate identical to the one used for the thin film deposition was used as a reference for the transmittance scan. However, the reflectance scan was taken at an incident angle of 5° with Al-mirror as reference. All the measurements were carried out at room temperature.

DC electrical conductivity measurements of PYR.B films were carried out in dark at the temperature range from 303 to 433 K, using an electrometer (Keithley 617A) with a high impedance of 10^{14} Ω. The temperature was measured directly by means of chromel–alumel thermocouple connected to hand-held digital thermometer.

The measurements of the current density–voltage (*J–V*) characteristics in dark were taken using high internal impedance electrometer Keithley 617A Source/Measure unit for dc measurement via equipped suitable coaxial cable.

The *I–V* curve tracer type 577 D1 Tektronix, USA was used to check the characteristics of the device under dark and illumination.

The source of light was a 500 W halogen lamp containing iodine vapor and tungsten filament. The intensity of light was calibrated with a solar power meter (TM-206, Taiwan). The intensity of light was varied by changing the voltage across the lamp.

2.2.1. Measurement of the color parameters

The tristimulus values *X*, *Y* and *Z* for any color in the visible spectrum range, 400–700 nm from the numerical values of reflectance spectrum (*R*) were calculated according to the colorimetric method (CIE, 1986) [28]. The chrometicity coordinates *x*, *y* and *z* to designate a color are given by

$$x = \frac{X}{X+Y+Z} \quad (1a)$$

$$y = \frac{Y}{X+Y+Z} \quad (1b)$$

$$z = \frac{Z}{X+Y+Z} \quad (1c)$$

where x + y + z = 1

For color parameters measurements, the brightness (L^*), the color constants (a^*) and (b^*), the whiteness index (W) and the yellowness index (Y_e) can be estimated by using the CIE relations (CIE, 1986)

$$L^* = 10(y)^{\frac{1}{2}} \quad (2)$$

$$a^* = 17.5\,\frac{\left[\left(\frac{x}{0.9804}\right) - y\right]}{y^{\frac{1}{2}}} \quad (3)$$

$$b^* = \frac{\left[\left(\frac{x}{0.9804}\right) - y\right]}{y^{\frac{1}{2}}} \quad (4)$$

$$W = 4\left[\left(\frac{z}{1.187031}\right) - 3y\right] \quad (5)$$

$$Y_e = 125\left[\frac{(x/0.9804) - (z/1.181031)}{y}\right] \quad (6)$$

2.2.2. Method of optical constants calculations

In order to calculate the optical constants namely the refractive index (n) and the absorption index (k) of the PYR.B. Thin films deposited onto the quartz transparent substrate is considered to be homogeneous using spectrophotometric measurements of transmittance and reflectance in the spectral range from 190 to 2500 nm, by using the following equations [29]:

$$\alpha = \frac{1}{d}\ln\left[\frac{(1-R^2)}{2T} + \sqrt{\frac{(1-R)^4}{4T^2} + R^2}\right] \quad (7)$$

$$k = \frac{\alpha\lambda}{4\pi} \quad (8)$$

$$n = \left(\frac{1+R}{1-R}\right) + \sqrt{\frac{4R}{(1-R)^2} - k^2} \quad (9)$$

where α is the absorption coefficient. When the thickness of film (d) is known, then the computation can be carried out and the optical constants can easily be calculated.

Table 1
The diffraction spacings d_{obs}, the Miller indices (hkl) and the relative intensity I/I_0.

2θ	$d_{obs.}$	$d_{cal.}$	I/I_0	(hkl)
16.01	5.53	5.53	33.48	(001)
18.11	4.90	4.90	100	(400)
22.72	3.91	3.91	49.57	(121)
23.85	3.73	3.73	2.15	(420)
26.14	3.41	3.41	25.80	(321)
28.22	3.16	3.16	16.87	(031)
35.13	2.55	2.56	3.19	(041)
36.27	2.47	2.47	4.97	(122)
36.50	2.46	2.46	15.11	(531)
37.21	2.41	2.41	9.71	(402)

3. Results and discussion

3.1. Structural and molecular characterizations

The crystalline structural characteristics were undertaken with the aim of determining the lattice parameters together with a complete list of the Miller indices and interplanar spacing for PYR.B. The X-ray diffraction patterns, XRD of the PYR.B in both powder and thin films are shown in Figs. 2(a) and (b). Fig. 2(a) reveals that a polycrystalline nature for the powder PYR.B. Applying the CRYSFIRE computer program [30] for indexing all the obtained diffraction lines, it was found that the minimized (2θ) values are in satisfactory agree with the observed values as shown in Table 1. Therefore, the

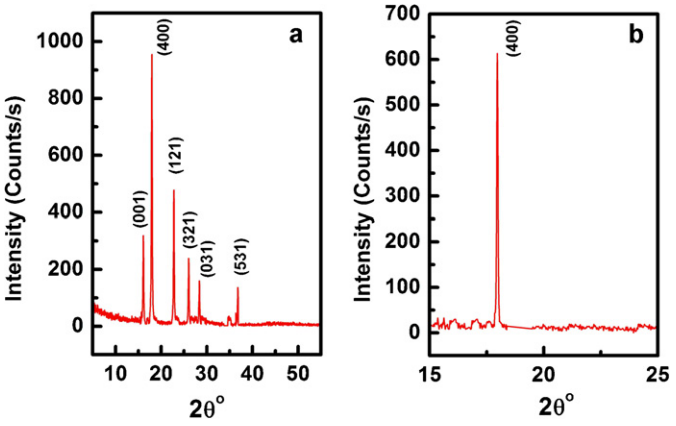

Fig. 2. (a) X-ray diffraction of powder PYR.B, (b) X-ray diffraction of PYR.B thin film.

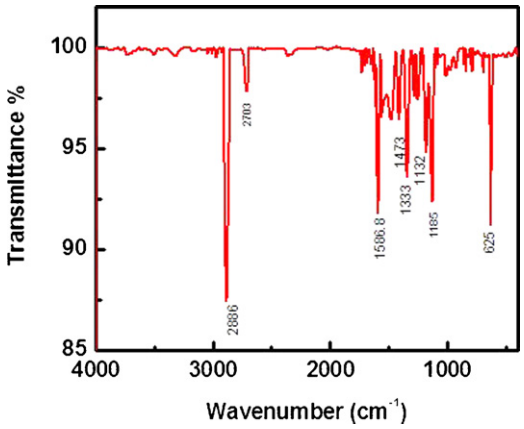

Fig. 4. Infrared spectrum of PYR.B film.

present deduced indexing can be accepted as orthorhombic crystal system with space group Pban and lattice parameters: $a = 19.599$ Å, $b = 11.539$ Å, $c = 5.536$ Å. Table 1 shows the values of Miller indices, *hkl*, for each diffraction peak together with the interplaner spacing (d_{hkl}) obtained by using CHECKCELL program [31].

On the other hand, the structure of the obtained PYR.B film is shown in Fig. 2(b). A strong peak oriented along the (4 0 0) direction was observed. This clearly indicates that the material of the prepared films has the same structure of PYR.B with orthorhombic type system.

Fig. 3 shows the scanning electron micrographs of the PYR.B thin films. As observed, a clearly almost uniform distribution and highly dense with large grain sizes in the range 5–10 μm were obtained. The microstructure consists of both smaller and large grains. The presence of small grains helped in the densification of the films. This type of morphology is desirable for boosting the photovoltaic response of the solar cells because larger grain sizes will reduce losses due to grain boundaries.

The Fourier transformation infrared technique (FTIR) is the unique characteristic of functional groups stacking the molecule and is found to be the most useful physical method of investigating and identifying the functional groups to know the molecular structure. FTIR was used to measure the transmittance spectra of PYR.B films deposited at room temperature (300 K) on nearly optically flat KBr substrate as shown in Fig. 4.

The strong bands in the region of 3000–2800 cm^{-1} can be associated with the aromatic C–H stretching vibration. The multiband absorptions of tertiary amine hydrochloride salts in the region 2700–2330 cm^{-1} are due to vibrations involving $N(C_2H_5)_2$ stretching. The bands at 2400–2300 cm^{-1} region can be attributed to the tertiary amine group. The bands in the region 1540–1620 cm^{-1} can be attributed to C–H bending vibrations of aromatic rings [32–34]. The vibrations involving CH_2 and CH_3 stretching (3000–2840 cm^{-1}) and bending modes (1470–1340 cm^{-1}) give rise to bands that are strong and characteristic in IR spectrum. Bands in the 1390–1340 cm^{-1} region can be assigned to the C_2H_5 bending mode. Bands in the region of 1180–1100 cm^{-1} in the IR spectrum can be associated with aromatic ether C–O symmetric and asymmetric stretching vibrations. Bands at 1132 and 625 cm^{-1} are characteristic of the ClO_4^- ion [33–36].

3.2. Fluorescence characterization

Remarkably, the PYR.B solid material showed a red fluorescence, which could be observed with the naked eye when the sample was illuminated with a hand-held UV lamp. Fig. 5 shows the emission spectrum of PYR.B. This spectrum shows a broad band at 569.65 nm which is in agreement with previously reported results [37]. This band is red-shifted and broadened in comparison with their absorption spectrum, which is characteristic of dimer and other aggregate states formed in the solid state [38]. According to previous studies on wide-gap organic semiconductors [39,40], this photoluminscent, PL emission can be attributed to radiative recombination of electron–hole pairs in the π–π^* localized states within

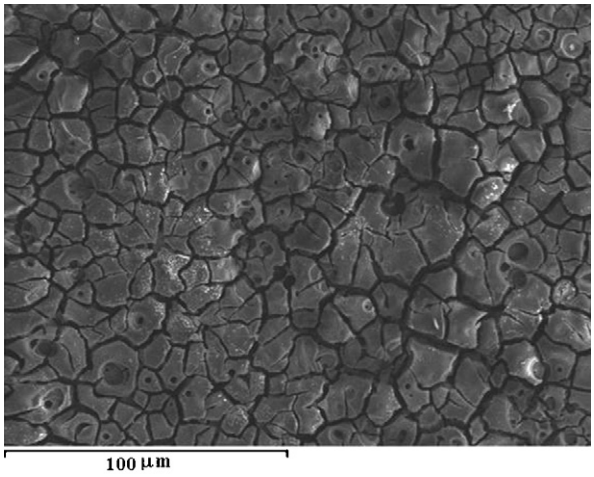

Fig. 3. Scanning electron micrograph of PYR.B film.

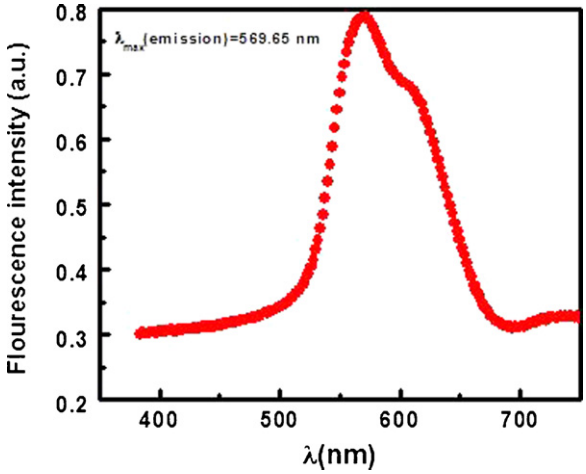

Fig. 5. Fluorescence spectrum of PYR.B.

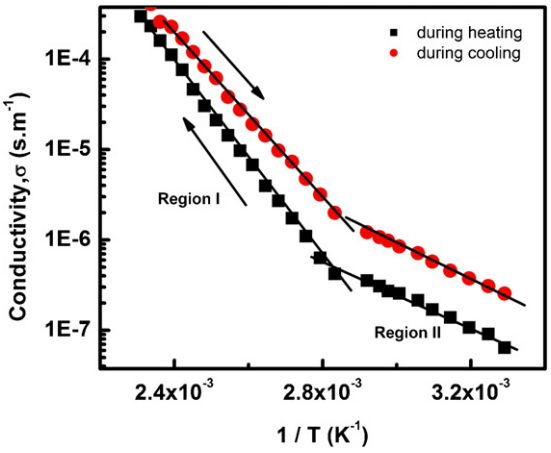

Fig. 6. Temperature dependence of dark electrical conductivity of PYR.B.

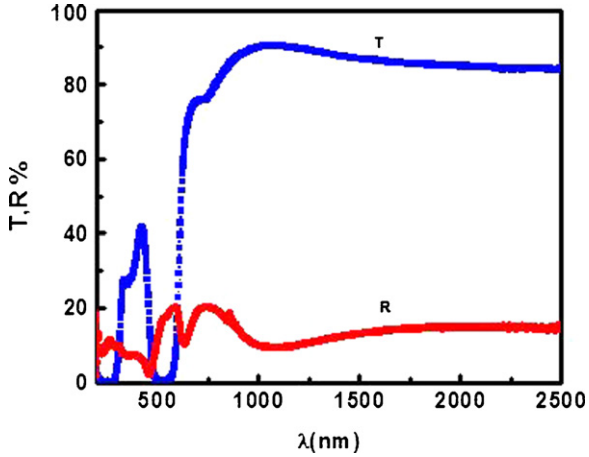

Fig. 7. Spectral dependence of transmittance and reflectance.

the band gap of the materials, rather than band-to-band transitions. Thus, PYR.B is promising with respect to the organic light emitting diodes (OLED) applications.

3.3. Electrical characteristics

D.C. electrical conductivity of PYR.B thin films was measured to determine the thermal activation energy. This study was carried out in the temperature range (303–433) K under air condition. The conductivity σ is measured at regular intervals of 5 K. The temperature dependence on conductivity is expressed as [41]

$$\sigma = \sigma_0 \exp\left(\frac{-\Delta E}{k_B T}\right) \quad (10)$$

where ΔE is the thermal activation energy and k_B is the Boltzmann's constant. A graph of log σ vs. $1/T$ for PYR.B films of thickness 600 nm is plotted as shown in Fig. 6 at different temperatures. The linear behavior of log (σ) vs. $1/T$ gives evidence for the semiconducting characteristics of the PYR.B films. Also, the conductivity exhibited irreversible changes for the films under heating and cooling during the measurement. There are two linear regions for the plots in Fig. 6 and the corresponding activation energies ΔE_1 and ΔE_2 are obtained above and below ~352 K, respectively. The values of activation energies are determined and collected in Table 2. It is seen from the table that as the activation energies for the film under cooling are less than that under heating. It is believed that two types of conduction mechanism occur, namely one in the first conduction region (I) and the other in the second conduction region (II). In both regions I and II, electrical conductivity is thermally activated owing to thermal excitation of charge carriers by changing the activation energy [42]. The observed increase in conduction can be associated with the number of the highly delocalized π-electrons along molecular backbone, whose presence is due to aromatic group of the compound. They are mainly responsible for the intramolecular electrical conduction, due to their thermal excitation. The π-electron mobility and the semiconducting behavior of PYR.B result from the transfer of this delocalized π-electrons [43].

Table 2
Thermal activation energies for the samples under heating and cooling.

	ΔE_1 (eV)	ΔE_2 (eV)
PYR.B under heating	1.05	0.38
PYR.B under cooling	0.91	0.35

3.4. Optical characteristics

Optical studies of PYR.B films were performed by measuring the transmittance and reflectance of the films deposited on quartz substrates in the wavelength region 190–2500 nm. Fig. 7 shows spectral dependence of the transmittance $T(\lambda)$ and reflectance $R(\lambda)$ of the PYR.B films. It is clear that the amount of light that gets transmitted through a thin film of PYR.B depends on the amount of reflection and absorption taking place along the light path. The transmittance behavior of all samples did not show multiple interferences, which indicate that, the PYR.B thin films have moderate absorption coefficients and thicknesses. Roughly, the spectrum can be divided into two regions: a transparent oscillating region, and a zone of strong absorption, where the transmittance decreases drastically. It could be noted that at longer wavelengths ($\lambda > 900$ nm), all films become transparent and no light is scattered or absorbed as non-absorbing region (i.e. $R + T = 1$). The inequality ($R + T < 1$) at shorter wavelengths ($\lambda < 900$ nm) known as absorbing region is due to the existence of absorption. The experimental points presented in this figure correspond with experimental data for the thickest deposited samples (600 nm).

The commission international De L·Eclairage (CIE) 1976 (L^*, a^*, b^*) color space provides a three dimensional representation for the perception of color stimuli (CIE, 1986).It is capable of representing all possible colors. This system uses three variables L^* which is the Luminance which represents the difference between light ($L = 100$) and dark ($L = 0$); a^* and b^* represent the color values on the red-green axis and blue-yellow axis, respectively. Whiteness index (W) and Yellowness index (Y_e) are also based on the distance of the color value in the color space from a nominal white point (i.e. a chromatic point which has $x = 0.333$, $y = 0.333$ and $z = 0.333$) [44].

Fig. 8 represents the spectral distribution of the tristimilus values (x, y and z) calculated from the values of reflectance as function of wavelength in the visible spectral range 400–700 nm. It is clear from the figure that the spectral distributions curves which represent the response of the three centers of stimulations posses by the retional cones i.e. there are three centers of stimulation within the eye. The values of X, Y and Z at the peak positions are recorded in Table 3. Moreover, the color parameters deduced for PYR.B are collected in Table 4.

Table 3
Peak position for the tristimulus values.

Tristimulus	X	Y	Z
Wavelength (nm)	440,575	550	440

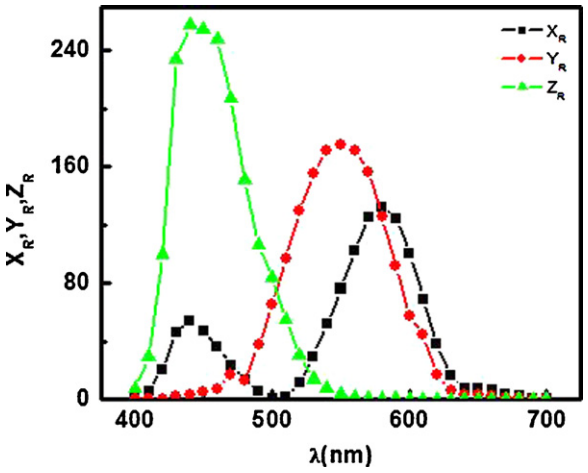

Fig. 8. Spectral dependence of tristimulus values of PYR.B.

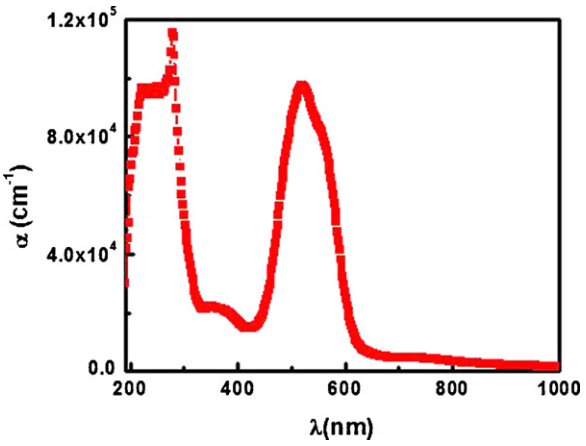

Fig. 10. Spectral dependence of absorption coefficient, α of PYR.B.

By using the relations 7, 8 and 9, the refractive, n and absorption indices, k of PYR.B films were determined from the measured transmittance and reflectance at normal light incidence. The spectral dependences of both $n(\lambda)$ and $k(\lambda)$ are plotted in Fig. 9. The extinction coefficients k of the thin films is very small at longer wavelengths, showing that the thin films are highly transparent. Evaluation of the refractive indices of optical materials is considerably important for the applications in integrated optics devices, such as switches, filters and modulation, in which the refractive index is a key parameter for the device design [45].

The refractive index, n of PYR.B thin film shows anomalous dispersion in the spectral range $400 > \lambda > 900$ nm and normal dispersion in the spectral range $900 > \lambda > 2500$ nm. This anomalous behavior is due to the resonance effect between the incident electromagnetic radiation and the electrons polarization, which leads to the coupling of electrons in PYR.B films to the oscillating electric field. Moreover, the peak in the refractive index corresponds to the optical energy gap of PYR.B film. The determined refractive index of PYR.B thin film is compared to the published of other xanthenes dyes [46–49] and tabulated in Table 5. As observed, a high refractive index value as compared to the some xanthenes derivatives. High value of the refractive index and then the dielectric constant can be attributed to the high bond strength, high density of atoms and high polarizability of PYR.B [50].

The absorption coefficient spectrum of PYR.B thin film is shown in Fig. 10. The well-known band of the PYR.B molecule, namely Q band appears in the region between 450 and 650 nm. As observed, PYR.B film shows one peak in this band at 520 nm. This may be generally been interpreted in terms of π–π^* excitation between bonding and anti-bonding molecular orbitals [51,52]. The other band appears in the UV region shows splitting at 222 nm and 277 nm. The first peak at 277 nm may be assigned to involves n–π^* transition and the shoulder at 222 nm can be assigned to the n–σ^* transitions of PYR.B molecule.

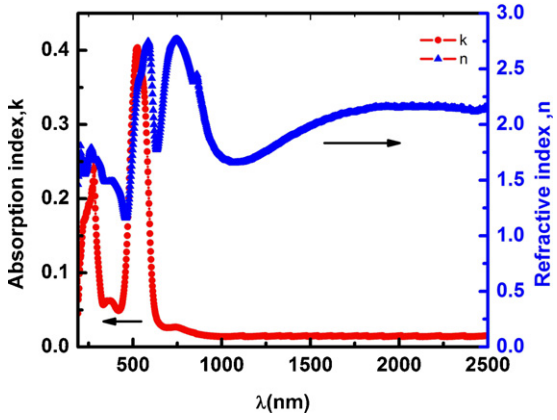

Fig. 9. Spectral dependence of optical constants n and k of PYR.B.

In Fig. 10 there are two absorption bands or edges are evident. The first edge was identified in the UV region with a wavelength range 275–335 nm and the second is located in the wavelength range 550–640 nm. These absorption edges correspond to optical transitions between occupied and unoccupied energy levels and are commonly referred in organic semiconductors as high occupied molecular orbital "HOMO" and low unoccupied molecular orbital "LUMO" levels. The optical transition between HOMO and LUMO energy levels can be described by the optical absorption coefficient, α, which is given by [53] as follows.

$$a = \left(\frac{A}{h\nu}\right)(h\nu - E_g)^m \tag{11}$$

where A is a constant, $h\nu$ is the incident photon energy and E_g is the band gap known as the energy difference between HOMO and LUMO. The exponent m is governed by the type of transition which can assume values of 2, 1/2, 1/3 or 3/2 depending on the nature of the band-to-band electronic transitions and the profile of the electron density in the valance and conduction bands. The experimental data have been fitted with the theoretical Eq. (11) for different values of m. As expected, the best fit is obtained for $m = 1/2$. This behavior indicated that the transitions are direct allowed transitions. The dependence of $(\alpha h\nu)^2$ on photon energy $h\nu$ near the absorption edge was plotted as shown in Figs. 11(a) and (b). Extrapolating the linear region of the curve to the value of $(\alpha h\nu)^2 = 0$ gives the value of energy gap. The obtained energy band gaps are 1.43 (Fig. 11(a)) and 2.07 eV (Fig. 11(b)) for the onset of the absorption spectrum and the fundamental energy gap, respectively. The lowest energy optical transition is referred to as the optical band gap or exciton level in solids.

The lowest energy optical transition is referred to as the optical band gap and the other is called the transport gap [54,55]. The calculated optical band gap (E_{opt}) is less than the calculated transport gap (E_t) and the difference is the exciton binding energy. It may be noted that the exciton binding energy is mainly depends on the dielectric constant of the material, molecular size and charge distribution on the molecule. Because of the molecular nature of organic solids and low dielectric constant the binding energy is high and lies in the range 0.5–1.7 eV [55]. In the present work the calculated binding energy is 0.64 eV which lies in the reported range. The determined energy gaps for PYR.B thin film are compared to the published for

Table 4
Color parameters deduced for PYR.B.

x	y	z	L^*	a^*	b^*	W	Y_e
0.2719	0.3626	0.3654	6.0218	−2.4783	0.6182	−3.1137	−6.6635

Table 5
Values of energy gap and refractive index for pyronine B films compared with other xanthene dyes derivatives.

Compound	Film treatment/condition	$E_g^{ind.allowed}$ (eV)	$E_g^{dir.allowed}$ (eV)	Refractive index	Reference
Pyronine B	Thermal evaporation	–	1.43 eV,2.07 eV	2.1	Present work
Rhodamine B	Drop casting technique	1.94	–	1.69	[46]
Pyronine B	Dip coating method	–	1.96	–	[47]
Pyronine G	Spin coating method	–	2.5 eV	–	[48]
Pyronine G	Thermal evaporation	1.87,2.25		1.71	[49]

other Xanthene dyes [46–49] as tabulated in Table 5. As observed, a common characteristic behavior for PYR.B and the most Xanthene dyes is the direct transitions [48,49], unlike the drop casting rhodamine B [46] and the thermally evaporated pyronine G material [49], where the transitions is an indirect allowed.

The complex refractive index $\tilde{n} = n + ik$ and dielectric function $\varepsilon = \varepsilon_1 + i\varepsilon_2$ characterize the optical properties of any solid material. The imaginary and real parts of dielectric constant of the films were also determined by the following relations [56]

$$\varepsilon_1 = n^2 - k^2 \quad (12)$$

and

$$\varepsilon_2 = 2nk \quad (13)$$

We calculated the imaginary and real parts of the dielectric constant as it is directly related to the density of states within the forbidden gap of the films. The real and imaginary parts of the dielectric constant of the film are respectively shown in Fig. 12. The real dielectric constant shows values larger than the imaginary dielectric constant in the studied photon energy. There are different behaviors for the two parts of the dielectric constant. The variation of the dielectric constant with photon energy indicates different interactions between photons and electrons in the films are produced in this energy range. These interactions are observed on the shapes of the real and imaginary parts of the dielectric constant and they cause formation of peaks in the dielectric spectra which depends on the material type.

3.5. Photovoltaic characteristics of Al/PYR.B/ITO junction

The current–voltage characteristics of Al/PYB.B/ITO device was measured by *I–V* curve tracer instrument in the dark and under illumination of 100 mW/cm^2, keeping ITO as positive with respect to Al electrode as shown in Fig. 13. It can be seen that the current value at a given voltage for the Al/PYB.B/ITO device under illumination is higher than that in dark. The dependence of dark current on voltage in the device exhibits a rectification effect. The rectification effect observed in dark *J–V* characteristics is due to the formation of Schottky barrier and ohmic contact at Al/PYR.B and ITO/PYR.B interfaces, respectively. The existence of a Schottky barrier at the Al/PYR.B interface is explained by the formation of the space charge region.

The *J–V* characteristic of Al/PYR.B/ITO device under 100 mW/cm^2 illumination at room temperature (300 K) is shown in Fig. 14. As seen from this figure, the Al/PYR.B/ITO device shows a photovoltaic behavior with a maximum open circuit voltage, V_{oc} of 500 mV and short-circuit current density, J_{sc} of 4 mA/cm^2. The illumination curve has a shape of an exponent with a series resistance and internal ohmic losses. The plot of electric out put power vs. voltage is also shown in Fig. 14. The electrical power increases with bias voltage and reaches a maximum value. The maximum point is called the maximum power point with coordinate ($P_{max} = J_{mp} \times V_{mp}$). Here J_{mp} and V_{mp} are maximum current density and voltage values of maximum power point, respectively. This maximum value represents the condition, where the solar

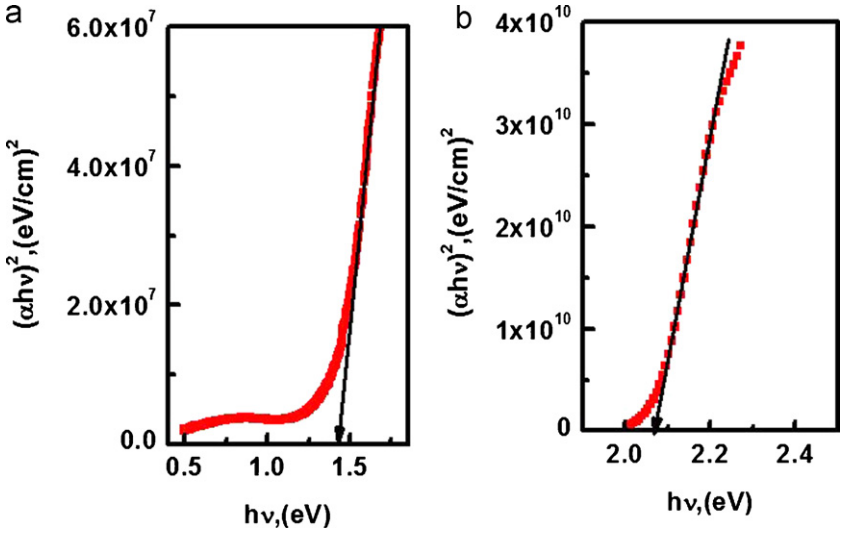

Fig. 11. (a, b) Photon energy dependence of $(\alpha h\nu)^2$ of PYR.B.

Table 6
Photovoltaic parameters of PYR.B films compared with other Xanthene dyes derivatives.

Compound	Film preparation	J_{sc} (mA/cm^2)	V_{oc} (V)	*FF*	V_{mp} (V)	J_{mp} (mA/cm^2)	Reference
Al/pyronine B/ITO	Thermal evaporation	4.00	0.50	0.35	0.30	2.66	Present work
Al/pyronine B/ITO	Spin coating	4.8×10^{-3}	1.00	0.44	0.55	3.84×10^{-3}	[57]
Oxazine/*n*-Si	Thermal evaporation	3.25	0.42	0.35	0.27	1.32	[58]

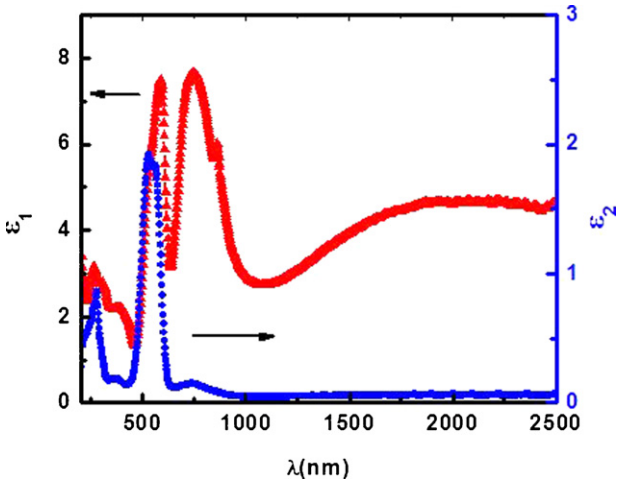

Fig. 12. Spectral dependence of the dielectric constants ε_1 and ε_2 of PYR.B.

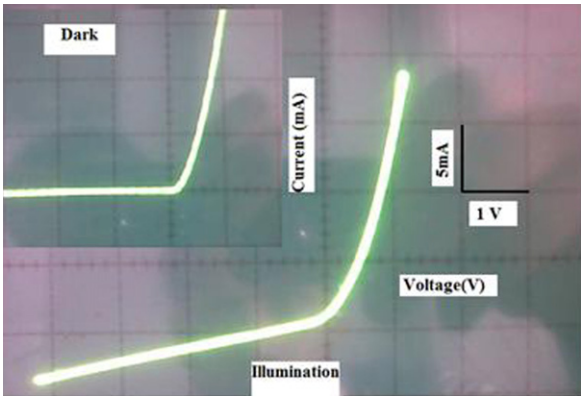

Fig. 13. *I–V* characteristics under dark and illumination of 100 mW/cm^2 of PYR.B.

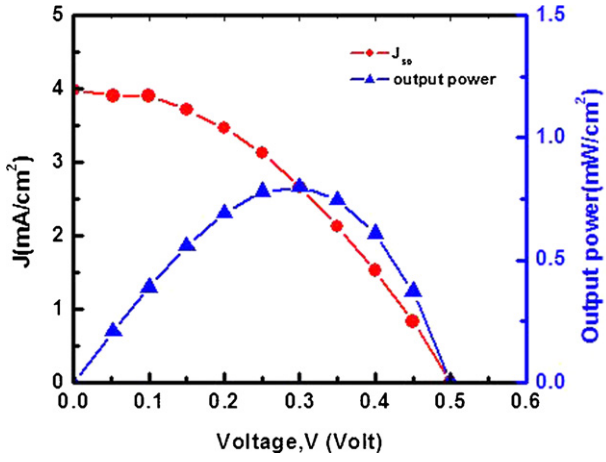

Fig. 14. Current–voltage characteristics and output power under illumination of 100 mW/cm^2.

cell can deliver its maximum power to an external load. The V_{mp} and J_{mp} values for Al/PYR.B/ITO device were found to be 300 mV and 2.66 mA/cm^2, respectively. Fill Factor, FF is found to be 0.35 for solar cell and furthermore, is measure of the closeness of the Al/PYR.B/ITO *J–V* curve to the rectangular shape and this value depends on the solar cell device and structure. The determined photovoltaic parameters for PYR.B thin film are compared to the other published Xanthene dyes [57,58] as tabulated in Table 6. As observed, a higher short circuit current density and maximum power intensity, V_{mp} and J_{mp} as compared to some Xanthene dye derivatives devices [57,58].

Since the absorption is highest at the peaks, only fraction of the light illuminating through the ITO side can reach the Schottky barrier (Al/PYR.B interface) and generate few excitons leading to low photocurrent. The barrier itself is not within a diffusion length of the carriers generated at the ITO surface, and as a result carriers generated near the ITO surface will be lost due to the recombination or trapping during the diffusion through PYR.B layer, toward the Al/PYR.B interface. At the wavelength with low absorption constant, the light can penetrate deeper near to the Al/PYR.B interface. Thus, more excitons will be generated near the Al/PYR.B interface, allowing more excitons to reach the Al/PYR.B interface resulting the higher photocurrent due to the exciton dissociation into free carriers under the effect of the built electric field at the interface. When the light is illuminating through Al electrode at peak wavelength, most of the excitons will be generated at Al/PYR.B interface and dissociate into free carriers resulting in a higher photocarriers [59]. Since the Al layer in our device is thick and not enough transparent, only small fraction of light irradiating from Al side can penetrate into the interface. Therefore, this is smaller in comparison to the photocurrent obtained illuminating through the ITO side. The above results suggest that the PYR.B behaves as p-type organic semiconductor which form the Schottky barrier Al/PYR.B interface, while ohmic contact at ITO/PYR.B interface.

The dependence of the short circuit current density J_{sc} and open circuit voltage, V_{oc} on the incident light intensity; *P* when illuminated through ITO was also examined as shown in Fig. 15(a) and (b). The open circuit voltage increases logarithmically with illumination intensity *P* at high excitation levels (Fig. 15(a)). The deviation from the logarithmic dependence at low intensity is principally due to the shunt current of the device. The dependence of J_{sc} on *P* for the device follows the relation $J_{sc} \propto P^m$, where the exponent $m < 1$. This is common behavior for the organic photovoltaic devices and could be explained by taking into account the model based on the combined effect of trap and recombination centers [60].

The variation of short circuit current density, J_{sc} with incident light intensity, *P* for Al/PYR.B/ITO devices is shown in Fig. 15(b). The J_{sc} shows a sublinear dependence with light intensity (*P*) that can be expressed as [61]

$$J_{sc} = BP^m \tag{14}$$

where B is a constant and *m* is the power factor which is equal to 0.92 for PYR.B based devices. The observed value of power factor less than unity is commonly associated with the presence of the trap centers within the band gap [53].

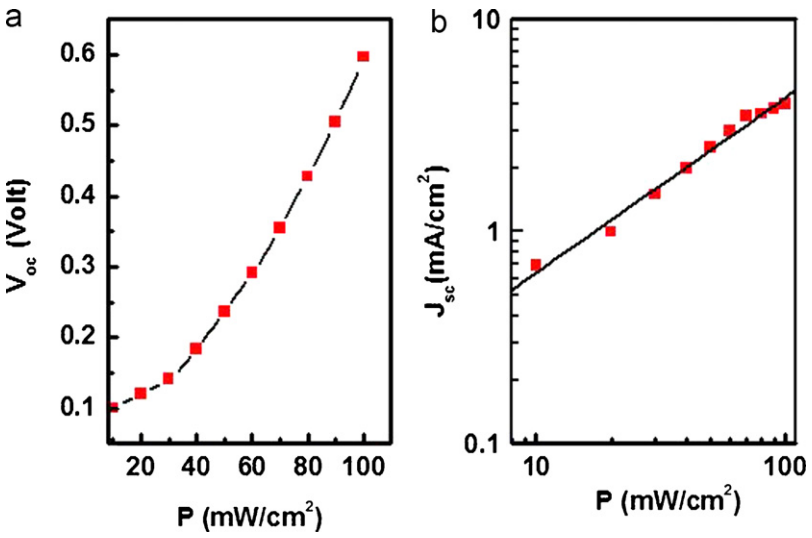

Fig. 15. (a) Open circuit voltage vs. power intensity, (b) short circuit current density vs. power intensity.

4. Conclusions

The XRD patterns obtained for PYR.B powder and thin films confirm that the material is polycrystalline with orthorhombic structure. Miller indices, *hkl*, values for each diffraction peak were also calculated. XRD obtained for PYR.B thin film confirmed that the as-deposited film is crystallized with preferred (4 0 0) orientation. Room temperature PL has been observed from PYR.B in the visible range. Two thermal activation energies are obtained from the temperature dependence of the dark electrical resistivity. The calculated optical band gap (E_{opt}) is less than the calculated transport gap (E_t) and the difference, 0.64 eV, is due to the exciton binding energy. From *J–V* characteristics in the dark, it is found that the device shows rectification effect due to the formation of a Schottky barrier at the Al/PYR.B interface. The results also show that the excitons produced within the diffusion length of the carrier can be diffused in the barrier region and subsequently dissociate into free carriers. The V_{mp}, J_{mp} and *FF* values for Al/PYR.B/ITO device were found to be 300 mV, 2.66 mA/cm^2 and 0.35, respectively. The observed light intensity dependence of the short circuit current density is commonly associated with the presence of the trap centers within the band gap.

Acknowledgments

This work was carried out through the collaboration between Department of Physics, Faculty of Education, Ain Shams University and Biophysics Department, Faculty of Science, Cairo University, Egypt.

References

[1] O. Gulu, A. Turut, J. Alloys Compd. 509 (2011) 571.
[2] M.M. El-Nahass, A.M. Farid, A.A. Atta, J. Alloys Compd. 507 (2010) 112.
[3] A. Sertap Kavasoglu, F. Yakuphanoglu, N. Kavasoglu, O. Pakma, O. Birgi, S. Oktik, J. Alloys Compd. 492 (2010) 421.
[4] S. Rasouli, S.J. Moeen, J. Alloys Compd. 509 (2011) 1915.
[5] M.M. El-Nahass, T.E. Youssef, J. Alloys Compd. 503 (2010) 86.
[6] A.A.M. Farag, I.S. Yahia, Synth. Met. 161 (2011) 32.
[7] V. Chithambaram, S. Jerome Das, S. Krishnan, J. Alloys Compd. 509 (2011) 4543.
[8] A.A.M. Farag, B. Gunduz, F. Yakuphanoglu, W.A. Farooq, Synth. Met. 160 (2010) 2559.
[9] M.M. El-Nahass, A.H. Ammar, A.A. Atta, A.A.M. Farag, E.F.M. El-Zaidia, Opt. Commun. 284 (2011) 2259.
[10] M.M. El-Nahass, A.H. Ammar, A.H. Ammar, A.A.M. Farag, A.A. Atta, E.F.M. El-Zaidia, Solid State Sci. 13 (2011) 596.
[11] M.M. El-Nahass, A.F. El-Deeb, H.S. Metwally, A.M. Hassanien, Mater. Chem. Phys. 125 (2011) 247.
[12] H.M. Zeyada, M.M. El-Nahass, I.K. El-Zawawi, M. El-Menyawy, J. Phys. Chem. Solids 71 (2010) 867.
[13] Z. Feng, Y. Hou, D. Lei, Renew. Energy 35 (2010) 1175.
[14] G. Xie, P. Sun, X. Yan, X. Du, Y. Jiang, Sens. Actuators, B 145 (2010) 373.
[15] J. Mary Linet, S. Dinakaran, S. Jerome Das, J. Alloys Compd. 509 (2011) 3832.
[16] N. Venkatramaiah, N. Veeraiah, R. Venkatesan, J. Alloys Compd. 509 (2011) 2797.
[17] H. Xu, Y. Xiao, X. Rao, Z. Dou, W. Li, Y. Cui, Z. Wang, G. Qian, J. Alloys Compd. 509 (2011) 2552.
[18] S.K. Sharma, A.I. Inamdar, B.G. Hyunsik Im, P.S. Kim, Patil, J. Alloys Compd. 509 (2011) 2127.
[19] R. Liu, Y. Liu, C. Liu, S. Luo, Y. Teng, L. Yang, R. Yang, Q. Cai, J. Alloys Compd. 509 (2011) 2434.
[20] J. Mou, W. Zhang, J. Fan, H. Deng, W. Chen, J. Alloys Compd. 509 (2011) 961.
[21] S.V. Vasyluk, O.O. Viniychuk, Ye.M. Poronik, Yu.P. Kovtun, M.P. Shandura, V.M. Yashchuk, O.D. Kachkovsky, J. Mol. Struct. 990 (2011) 6.
[22] T. Nemoto, K. Obuchi, S. Tamura, T. Fukuyama, Y. Hamada, Tetrahedron Lett. 52 (2011) 987.
[23] X. Yang, M. Zhao, G. Wang, Sens. Actuators, B 152 (2011) 8.
[24] J. Luan, M. Li, K. Ma, Y. Li, Z. Zou, Tetrahedron 67 (2011) 1091.
[25] S. Murcia López, M.C. Hidalgo, J.A. Navío, G. Colón, J. Hazard. Mater. 185 (2011) 1425.
[26] S. Shaun Murphree, Prog. Heterocycl. Chem. 22 (2011) 21.
[27] H.S. Soliman, A.A.M. Farag, N.M. Khosifan, M.M. El-Nahass, Thin Solid Films 516 (2008) 8678.
[28] CIE Publication No. 15.2, Colorimetry, 2nd ed., mCIE Central Bureu Kegelgasse 27 A-1030, Wien, Austria, 1986.
[29] M.M. El-Nahass, A.A. Atta, H.E.A. El-Sayed, E.F.M. El-Zaidia, Appl. Surf. Sci. 254 (2008) 2458.
[30] R. Shirley, The CRYSFIRE System for Automatic Powder Indexing: User's Manual, The Lattice Press, Guildford, Surrey GU2 7NL, England, 2000.
[31] J. Laugier, B. Bochu, LMGP-Suite Suite of Programs for the Interpretation of X-ray 16 Experiments, ENSP/Laboratoire des Materiaux et du Genie Physique, BP46.38042, Saint Martin d'Heres, France, 2000.
[32] Y.T. Chang, C.F. Shu, C.M. Leu, K.H. We, J. Polym. Sci. Part A: Polym. Chem. 41 (2003) 3726.
[33] J.Y. Wang, G.X. Liao, C. Liu, X.G. Jian, J. Polym. Sci. Part A: Polym. Chem. 42 (2004) 6089.
[34] T. Gavrilko, R. Fedorovich, G. Dovbeshko, A. Marchenko, A. Naumovets, V. Nechytaylo, G. Puchkovska, L. Viduta, J. Baran, H. Ratajczak, J. Mol. Struct. 704 (2004) 163.
[35] W.H.Abd. Majid, T.H. Richardson, D. Lacey, A. Topacli, Thin Solid Films 376 (2000) 225.
[36] U.S. Bhansali, M.A. Quevedo Lopez, H. Jia, H.N. Alshareef, D. Cha, M.J. Kim, B.E. Gnade, Thin Solid Films 517 (2009) 5825.
[37] A.K. Dutta, Solid State Commun. 95 (1995) 159.
[38] M. Re¸barz, M. Wojdyła, W. Bała, Z. Łukasiak, Opt. Mater. 30 (2008) 774.
[39] Y. Li, Y. Liu, J. Guo, F. Wu, W. Tian, B. Li, Y. Wang, Synth. Met. 118 (2001) 175.
[40] Y. Wang, J.C. Zhao, S. Zhang, Q. Liu, X. Wu, J. Non-Cryst. Solids 351 (2005) 1477.
[41] M. Serin, O. Cankurtaran, F. Yilmaz, J. Optoelectron. Adv. Mater. 5 (2003) 569.
[42] V. Bertolasi, L. Nanni, P. Gilli, V. Ferretti, Y.M. Issa, O.E. Sherif, New J. Chem. 18 (1994) 251.
[43] F. Yakuphanoglu, I. Erol, Physica B 352 (2004) 378.
[44] R.W. Gerbech, X. Zhou, S.F. Mc Clanehen, Am. J. Dent. (2002) 19A.

[45] H. Neumann, W. Horig, E. Reccius, H. Sobotta, B. Schumann, G. Kuhn, Thin Solid Films 61 (1979) 13.
[46] A.A.M. Farag, I.S. Yahia, Opt. Commun. 283 (2010) 4310.
[47] P. Balraju, P. Suresha, Manish Kumarb, M.S. Royb, G.D. Sharma, J. Photochem. Photobiol. A 206 (2009) 53.
[48] G.D. Sharma, Shailendra Sharma, M.S. Roy, Mater. Sci. Eng. B 110 (2004) 135.
[49] H.S. Soliman, A.M.A. El-Barry, S. Yaghmour, T.S. Al-Solami, J. Alloys Compd. 481 (2009) 390.
[50] P.S. Ho, J. Leu, W.W. Lee, Low Dielectric Constant Materials for IC Applications, Springer Series in Advanced Microelectronics, vol. 9, Springer-Verlag, Berlin, Heidelberg, 2003.
[51] A.T. Davidson, J. Chem. Phys. 77 (1982) 162.
[52] T. Fujii, H. Nishikiori, T. Tamura, Chem. Phys. Lett. 233 (1995) 424.
[53] A.A.M. Farag, Opt. Laser Technol. 39 (2007) 728.
[54] D. Cahen, A. Kahn, E. Umbach, Mater. Today 8 (2005) 32.
[55] K. Pabitra, N. Nayak, Periasamy, Org. Electron. 10 (2009) 1396.
[56] A. El-Korashy, H. El-Zahed, M. Radwan, Physica B 334 (2003) 75.
[57] G.D. Sharma, S. Sharma, M.S. Roy, Mater. Sci. Eng. B 110 (2004) 135.
[58] A.A.M. Farag, E.A.A. El-Shazly, M. Abdel Rafea, A. Ibrahim, Sol. Energy Mater. Sol. Cells 93 (2009) 853.
[59] G.D. Sharma, V.S. Choudhary, M.S. Roy, Sol. Energy Mater. Sol. Cells 91 (2007) 1087.
[60] G.D. Sharma, M. Roy, M.S. Roy, Mater. Sci. Eng. B 104 (2003) 15.
[61] F. Yakuphanoglu, J. Alloys Compd. 494 (2010) 451.